
Heavy Ion Collisions

Raimond Snellings¹

NIKHEF, Amsterdam, The Netherlands

Summary. Lattice QCD predicts a phase transition between hadronic matter and a system of deconfined quarks and gluons (the Quark Gluon Plasma) at high energy densities. Recent results from the Brookhaven Relativistic Heavy Ion Collider (RHIC) dedicated to the study of QCD at extreme densities will be discussed and compared to measurements obtained at the CERN Super Proton Synchrotron (SPS).

1 Introduction

Quantum Chromo Dynamics (QCD) provides, as part of the standard model, a very successful description of strong interaction processes involving large momentum transfer. However, from first principles several important aspects of QCD are still poorly understood. Examples are color confinement, chiral symmetry restoration and the structure of the vacuum. Better understanding of these concepts can be obtained if we are able to study quarks and gluons in a deconfined state, the so-called Quark Gluon Plasma (QGP).

Such a deconfined state might be created in the laboratory in heavy-ion collisions at the highest energies. Theoretical guidance for this comes from Lattice QCD calculations. Lattice QCD predicts that at an energy density $\epsilon \approx 1 \text{ GeV}/\text{fm}^3$, corresponding to a temperature of about 170 MeV, the system undergoes a phase transition from nuclear matter to a deconfined system of quarks and gluons.

Figure 1a shows the energy density divided by the fourth power of the temperature, T , versus the temperature from a lattice calculation [1]. This figure shows that in between 150-200 MeV the energy density increases rapidly which is indicative of a phase transition where at high temperature the quarks and gluons become the relevant degrees of freedom. The figure also indicates where according to our current understanding the different heavy-ion machines are located on this diagram. These calculations are done with zero baryon chemical potential, μ_B , reflecting the conditions of the early universe. Small values of the chemical potential are obtained at RHIC collider energies whereas at

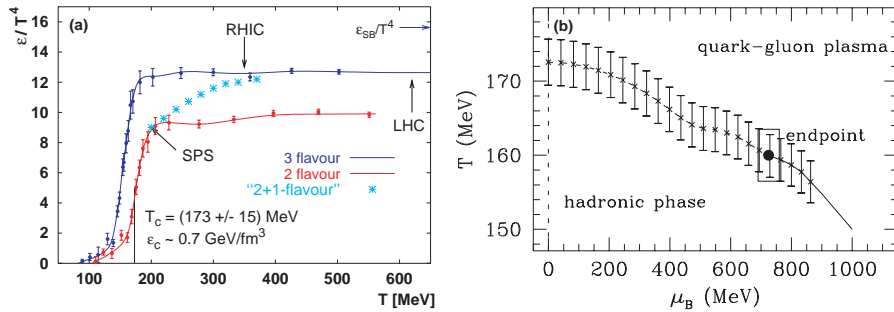


Fig. 1. *a)* Energy density divided by T^4 versus T at $\mu_B = 0$ [1]. *b)* Transition temperature as a function of μ_B [2]. The dotted line illustrates the rapid crossover while the solid line illustrates the first order phase transition.

lower energies, e.g. AGS and SPS, the value of μ_B is large. In Fig. 1b the relation between the transition temperature and the chemical potential from recent lattice calculations [2] is shown. The calculation indicates that the transition temperature decreases with increasing μ_B and furthermore that at low μ_B the transition from the hadronic phase to the QGP is a rapid crossover (dotted line) while at large μ_B a first order transition should take place (full line).

2 The Relativistic Heavy Ion Collider (RHIC)

Heavy-ion physics entered a new era with the advent of the Relativistic Heavy Ion Collider (RHIC) at Brookhaven National Laboratory. RHIC is a versatile collider providing collisions with different ion species (ranging from protons to gold) at a wide range of center of mass energies $\sqrt{s_{NN}}$. In the four years of operation collisions were provided for Au+Au at 19.7, 130 and 200 GeV, p+p at 200 GeV and d+Au at 200 GeV. Note that the top center of mass energy for p+p is 500 GeV at RHIC. For details on the machine and the detectors (BRAHMS, PHENIX, PHOBOS, STAR), see [3, 4].

3 Event Characterization

Heavy ions are extended objects and the system created in a head-on collision is different from that in a peripheral collision. Therefore, collisions are categorized by their centrality. Theoretically the centrality is characterized by the impact parameter \mathbf{b} which, however, is not a direct observable. Experimentally, the collision centrality can be inferred from the measured particle multiplicities if one assumes that this multiplicity is a monotonic function of \mathbf{b} (see Fig. 2a). Another way to determine the event centrality is to measure

the energy carried by the spectator nucleons (which do not participate in the reaction) with Zero Degree Calorimetry (ZDC), shown in Fig. 2b. A large (small) signal in the ZDCs thus indicates a peripheral (central) collision.

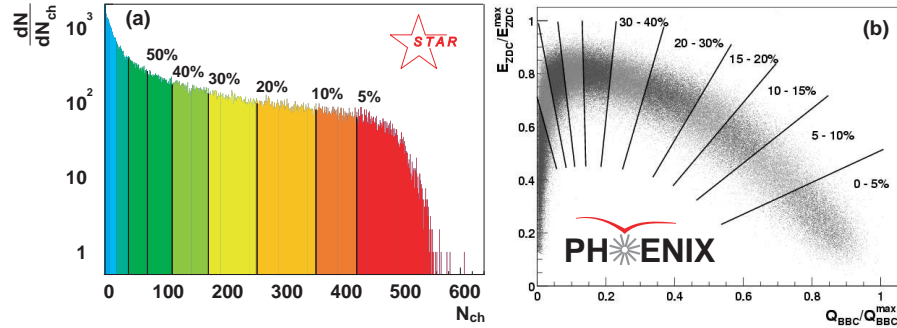


Fig. 2. a) Multiplicity distribution measured in STAR [5]. The different colors denote the different fractions of the cross section. b) ZDC signal versus multiplicity, measured by PHENIX [6].

Two other measures of the centrality which are often used are the number of wounded nucleons and the equivalent number of binary collisions. These numbers are related to the impact parameter \mathbf{b} using a realistic description of the nuclear geometry in a Glauber calculation, see Fig. 3. Phenomenologically it is found that soft particle production scales with the number of participating nucleons whereas hard processes scale with the number of binary collisions.

4 Low- p_t Observables

Examples of global observables which provide important information about the created system are the particle multiplicity and the transverse energy. Figure 4 shows the transverse energy versus the collision centrality as measured at $\sqrt{s_{NN}} = 130$ GeV by the PHENIX collaboration [7]. This measurement allows for an estimate of the energy density as proposed by Bjorken [8]

$$\epsilon = \frac{1}{\pi R^2} \frac{1}{c\tau_0} \frac{dE_T}{dy},$$

where R is the nuclear radius and τ_0 is the effective thermalization time (0.2-1.0 fm/c). From the measured $\langle dE_T/d\eta \rangle = 503 \pm 2$ GeV it follows that ϵ is about 5 GeV/fm³ at RHIC. This is much larger than the critical energy density of 1 GeV/fm³ from Lattice QCD (see Fig. 1).

Figure 5 shows the charged particle multiplicity distributions versus the pseudorapidity η measured by PHOBOS at three different energies [9]. The

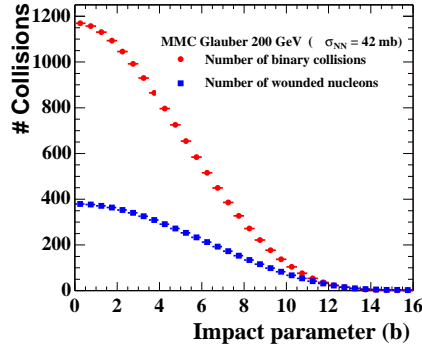


Fig. 3. Number of wounded nucleons and binary collisions versus impact parameter.

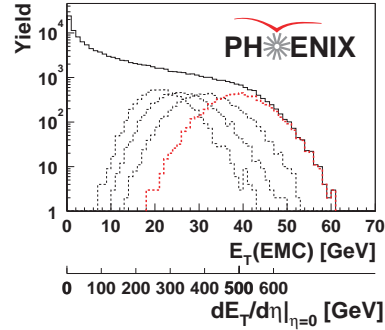


Fig. 4. Transverse energy as a function of centrality as measured by PHENIX [7].

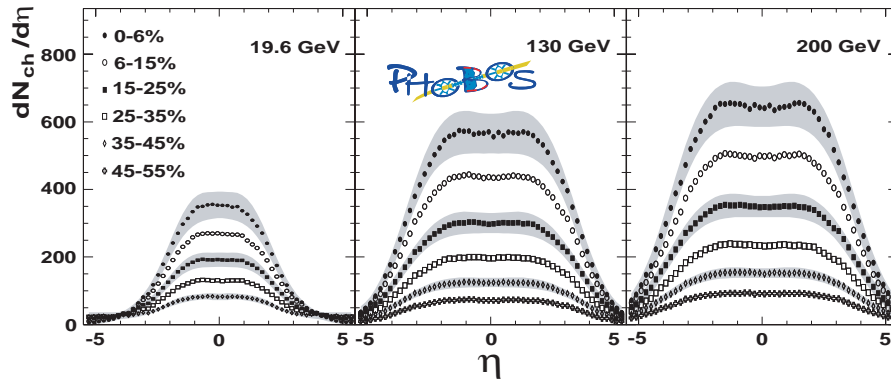


Fig. 5. Multiplicity versus pseudo-rapidity for 19.6, 130 and 200 GeV measured by PHOBOS [9].

gross features of the particle multiplicity distributions are described by a similar behavior of the tails (limiting fragmentation) and a plateau at mid-rapidity consistent with a boost invariant region of $\Delta y \approx 1$. Notice that in total about 5000 charged particles are produced in the most central Au+Au collisions at the top RHIC energy.

4.1 Particle Yields

The integrated yield of the various particle species provides information on the production mechanism and the subsequent inelastic collisions. A very successful description of the relative particle yields is given by the thermal model. In Fig. 6 the particle yield ratios measured at RHIC are plotted and compared

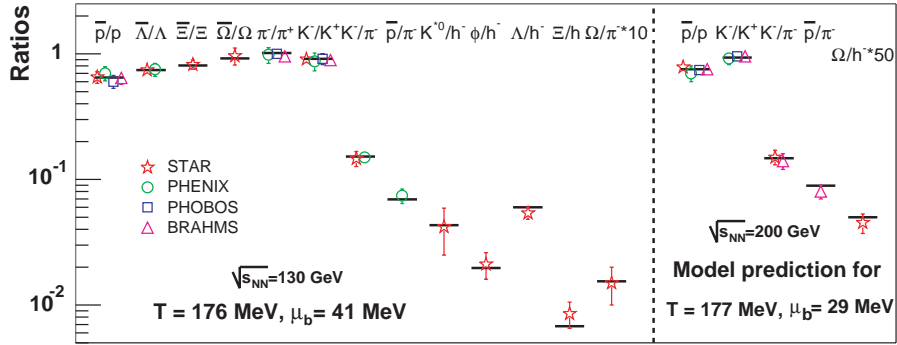


Fig. 6. Particle yield ratios at RHIC compared with a thermal model [11].

to values from a thermal model fit [11]. The results from the fit show that all particles ratios are consistent with a single temperature and single chemical potential in a thermal description. The temperature obtained in this way, 176 MeV, is called the chemical freeze-out temperature. Figure 7a shows the rela-

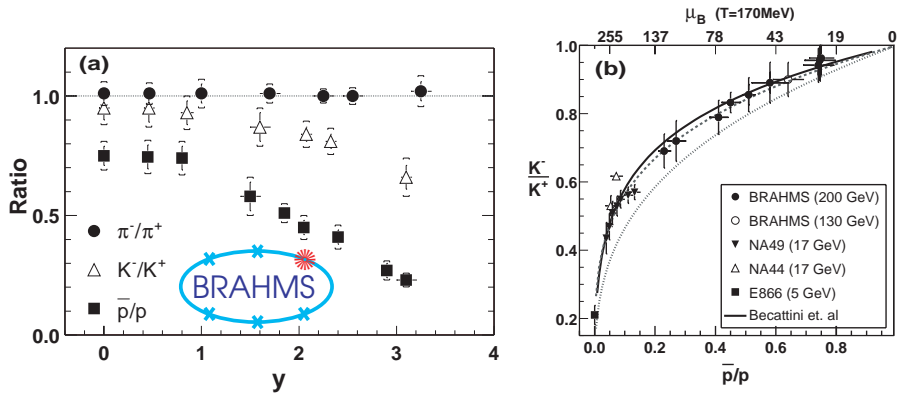


Fig. 7. a) Particle ratios versus rapidity measured by BRAHMS [10]. b) The ratio K^-/K^+ versus \bar{p}/p or, equivalently, μ_B .

tive particle ratios of pions, kaons and protons and their anti-particles versus rapidity [10]. For the protons and kaons the ratio drops rapidly for $y > 1$. Figure 7b shows the ratio of K^-/K^+ versus \bar{p}/p for AGS to RHIC energies. The decreasing ratio of \bar{p}/p as a function of rapidity can thus be understood from the changing baryon chemical potential at a constant chemical freeze-out temperature.

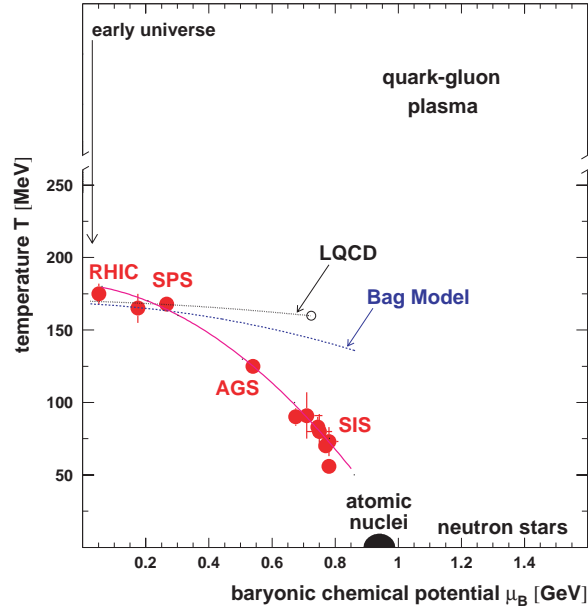


Fig. 8. Our current knowledge of the phase diagram [12]. Shown is the chemical freeze-out temperature versus μ_B obtained at different beam energies, which can be compared to the critical temperature from lattice QCD calculations.

Figure 8 shows the chemical freeze-out temperature obtained in the thermal model versus μ_B in the SIS to RHIC energy range. The chemical freeze-out temperature increases strongly from SIS to SPS energies above which it seems to saturate close to the phase boundary temperature from lattice calculations (see also Fig. 1b). This observation is not inconsistent with the scenario that the matter produced at SPS and RHIC energies was first thermalized in the deconfined quark-gluon plasma phase and subsequently expanded through the phase boundary into a thermal gas of hadrons. For a detailed overview of particle production and the thermal model see [13].

4.2 Spectra

The particle spectra provide much more information than the integrated particle yields alone. The particle yield as a function of transverse momentum reveal the dynamics of the collision, characterized by the temperature and transverse flow velocity of the system at kinetic freeze-out. Kinetic freeze-out corresponds to the final stage of the collision when the system becomes so dilute that all interactions between the particles cease to exist so that the momentum distributions do not change anymore. Figure 9a and b show the transverse momentum distributions at $\sqrt{s} = 17$ GeV from NA49 [14]. The

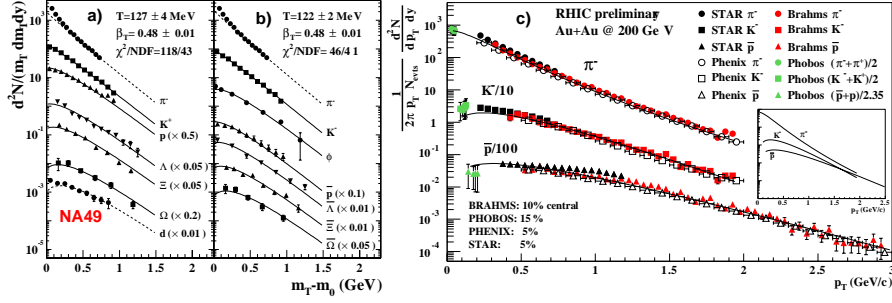


Fig. 9. NA49 (SPS) and RHIC low- p_t spectra [14, 15, 19, 18, 16, 17].

lines are a fit to the particle spectra with a hydrodynamically inspired model (blast wave). The fit describes all the particle spectra rather well which shows that these spectra can be characterized by the two parameters of the model: a single kinetic freeze-out temperature and a common transverse flow velocity. Figure 9c shows the combined pion, kaon and proton p_t -spectra from the four RHIC experiments. Also at these energies it follows from a common fit to all the spectra that the system seems to freeze-out with a similar temperature and transverse flow velocity as observed at SPS energies.

4.3 Azimuthal Correlations with the Reaction Plane

The nuclear overlap region, shown in gray in Fig. 10a, has in non-central collisions an almond like shape with its longer axis perpendicular to the reaction plane (the plane defined by the beam axis \mathbf{Z} , and the impact parameter \mathbf{b}). This particular shape leads to a pressure gradient which is different in and out of the reaction plane which, in turn leads to azimuthally asymmetric particle emission. The asymmetry can be described by:

$$E \frac{d^3 N}{d^3 p} = \frac{1}{2\pi} \frac{d^2 N}{p_t dp_t dy} \left[1 + \sum_{n=1}^{\infty} 2v_n \cos(n\phi') \right]$$

where ϕ' is the azimuthal angle with respect to the reaction plane and the coefficient of the second harmonic, v_2 , is called elliptic flow. The magnitude of v_2 and its p_t dependence allows for the extraction of the kinetic freeze-out temperature and the transverse flow velocity as function of emission angle.

Figure 10b shows the integrated value of v_2 versus beam energy. The magnitude of v_2 increases smoothly from AGS to the top RHIC energy. At the highest RHIC energies for the first time in heavy-ion collisions the value reaches qualitative agreement with prediction from hydrodynamic model calculations [21].

Figure 11 shows the measurement of v_2 versus p_t for pions and protons plus antiprotons. Due to transverse flow the p_t dependence of v_2 depends on

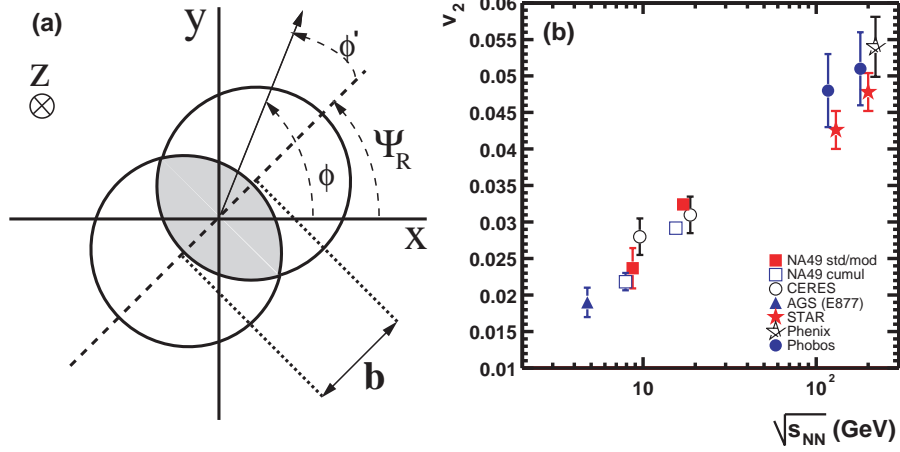


Fig. 10. *a)* Illustration of the nuclear overlap region in non-central heavy-ion collisions. *b)* Integrated value of v_2 versus beam energy [20].

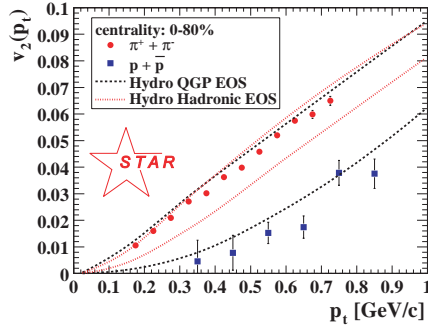


Fig. 11. $v_2(p_t)$ for pions and protons at $\sqrt{s_{NN}} = 130$ [23]. The lines are hydrodynamical model calculations [22].

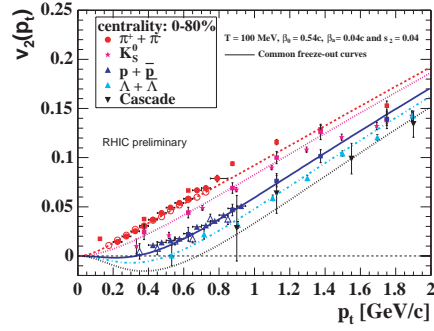


Fig. 12. $v_2(p_t)$ for identified particles compared to a blast wave fit [23, 24, 25, 26].

the particle mass as is evident from Fig. 11. Also shown in this figure are hydrodynamical model calculations using two different equations of state [22] corresponding a hadron gas and a QGP. It is seen that the QGP EOS shows the best agreement with the data. In Fig. 12 RHIC data on $v_2(p_t)$ [23, 24, 25, 26] for various particles are compared to a hydrodynamical inspired blast wave fit. The agreement of the data with this fit shows that the $v_2(p_t)$ for all particles can be described in terms of a single temperature and a ϕ -dependent transverse flow velocity. Furthermore, the magnitude and p_t dependence of the elliptic flow for the various particles suggest strong *partonic* interactions in an early stage of the collision and, perhaps, early thermalization of the system.

4.4 Hanbury-Brown Twiss Interferometry

Two-particle intensity interferometry, or the Hanbury-Brown Twiss [27] (HBT) effect, is a technique used to measure the size of an object emitting bosons. In heavy-ion collisions pion HBT has been used extensively to probe the space-time structure of the produced system.

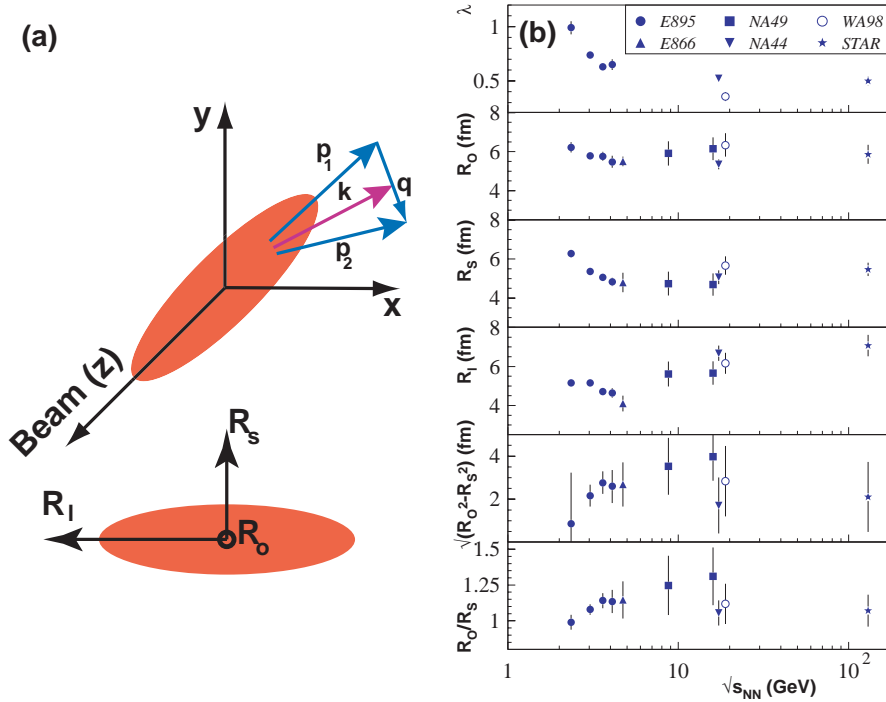


Fig. 13. *a) Coordinate system used in HBT. b) The energy dependence of π^- HBT parameters [28].*

For a given pair of pions, we can define their momentum difference, \mathbf{q} , and their momentum average, \mathbf{k} (see Fig. 13a). With these two vectors and the beam direction we can define the coordinate system used in HBT [29]: The longitudinal direction (R_l), which is along the beam direction \mathbf{z} . The outward direction (R_o), in the \mathbf{z}, \mathbf{k} plane and $\perp \mathbf{z}$. Finally the side-ward direction (R_s), $\perp \mathbf{z}$ and $\perp \mathbf{k}$. At low- p_t , for a boost-invariant source, the side-ward radius will correspond to the actual physical transverse (RMS) size of the source at kinetic freeze-out. At larger- p_t the source size reflects the region of homogeneity, due to the transverse flow of the system. The outward radius contains a mixture of the spatial and time extent of the source. Figure 13b shows the energy dependence of the π^- HBT radii [28]. The evolution of

the HBT radii shows a smooth dependence versus center of mass energy. The observed ratio R_o/R_s is part of the so-called ‘‘RHIC HBT puzzle’’. The value is very close to unity, which naively implies an almost instantaneous emission of particles. The models, which are successful in describing the measured spectra and elliptic flow, predict larger values for this ratio. However in a blast wave description the dependence of the HBT radii versus p_t is consistent with the large transverse flow deduced from the identified particle spectra and v_2 [30].

5 High- p_t observables

In heavy-ion collisions at RHIC, jets with transverse energies above 40 GeV are produced in abundance, providing a detailed probe of the created system. However the abundant soft particle production in heavy-ion collisions tends to obscure the characteristic jet structures. At sufficient high- p_t the contribution from the tails of the soft particle production becomes negligible and jets can be identified by their leading particles. It was proposed that a leading particle traversing a dense system would lose energy by induced gluon radiation (so called jet-quenching [31]). The amount of energy loss is in this picture directly related to the parton density (mainly gluons at RHIC) of the created system. Currently there are three observables sensitive to this energy loss as discussed in the next two subsections.

5.1 Single Inclusive Particle Yields

As mentioned above, the single inclusive particle yield at sufficiently high- p_t is dominated by the leading particles from jets. Figure 14a shows the π_0 spectra as measured in p+p at $\sqrt{s} = 200$ GeV. In the same figure also two NLO QCD calculations are shown. The ratio of the data to the theory shows that in p+p the π_0 spectrum is well described. In Fig. 14e the charged hadron spectra measured in Au+Au at $\sqrt{s_{NN}} = 200$ GeV and the p+p reference spectra at the same energy are shown. One of the observables suggested for measuring energy loss is the so called nuclear modification factor defined by

$$R_{AA}(p_t) = \frac{d^2\sigma_{AA}/dydp_t}{\langle N_{\text{binary}} \rangle d^2\sigma_{pp}/dydp_t},$$

where $d^2\sigma_{pp}/dydp_t$ is the inclusive cross section measured in p+p collisions (see Fig. 14a,e) and $\langle N_{\text{binary}} \rangle$ (see Fig. 3) accounts for the geometrical scaling from p+p to nuclear collisions. In the case that a Au+Au collision is an incoherent superposition of p+p collisions this ratio R_{AA} would be unity. Energy loss and shadowing would reduce this ratio below unity while anti-shadowing and the Cronin effect would lead to a value above unity. Figure 15b,c shows this ratio for charged particles and π_0 's in central Au+Au collisions at mid-rapidity. The ratio is well below one and at high- p_t the suppression is a factor

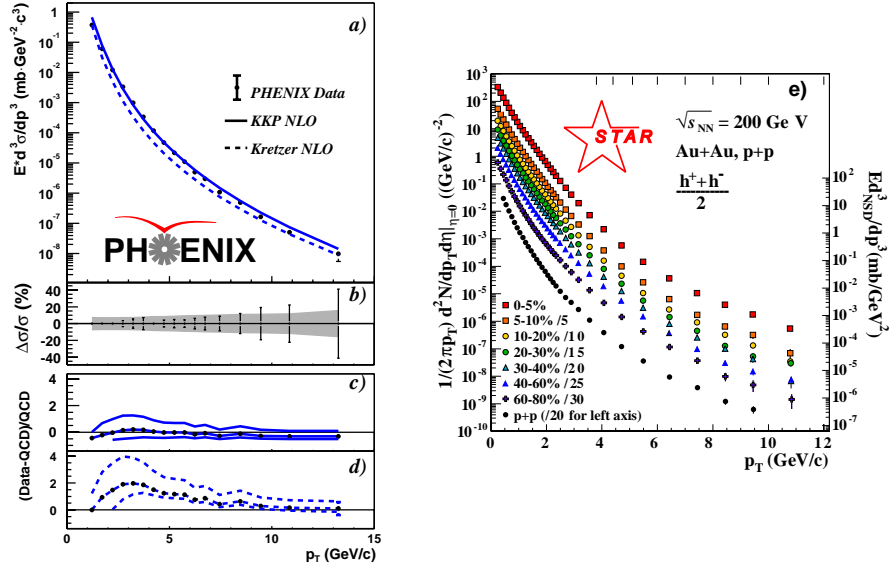


Fig. 14. *a-d)* π_0 spectra in $p+p$ [32] compared to NLO QCD calculations. *e)* Charged hadrons in $p+p$ and $Au+Au$ [33].

of 5. At intermediate p_t the charged particles and π_0 are both suppressed; however the magnitude differs by a factor of two. In Fig. 15d R_{AA} is plotted at more forward rapidities showing that the suppression also persists there.

To discriminate between energy loss and shadowing, d+Au collisions were measured. If the suppression is due to shadowing it should also be observed in the d-Au system. Figure 15a shows the d+Au spectra versus centrality and Fig. 15b,c the nuclear modification factor for charged particles and π_0 , respectively. It is clear that in d+Au interactions no suppression is observed. In fact, to the contrary, a small enhancement is seen consistent with the Cronin effect. From this observation it follows that the observed suppression in Au+Au collisions is due to final state interactions. The magnitude of the observed suppression at the top RHIC energy indicates, in the jet quenching picture, densities which are a factor 30 higher than in nuclear matter.

5.2 Azimuthal Correlations

In heavy-ion collisions, azimuthal correlations between particles can be used to study the effect of jet quenching in greater detail. The azimuthal correlations of two high- p_t particles from jets are expected to show a narrow near-side correlation and a broader away-side correlation. However, in the case of strong jet quenching the away-side jet would suffer significant energy loss and would be suppressed. Recently, CERES measured such a correlation function at the

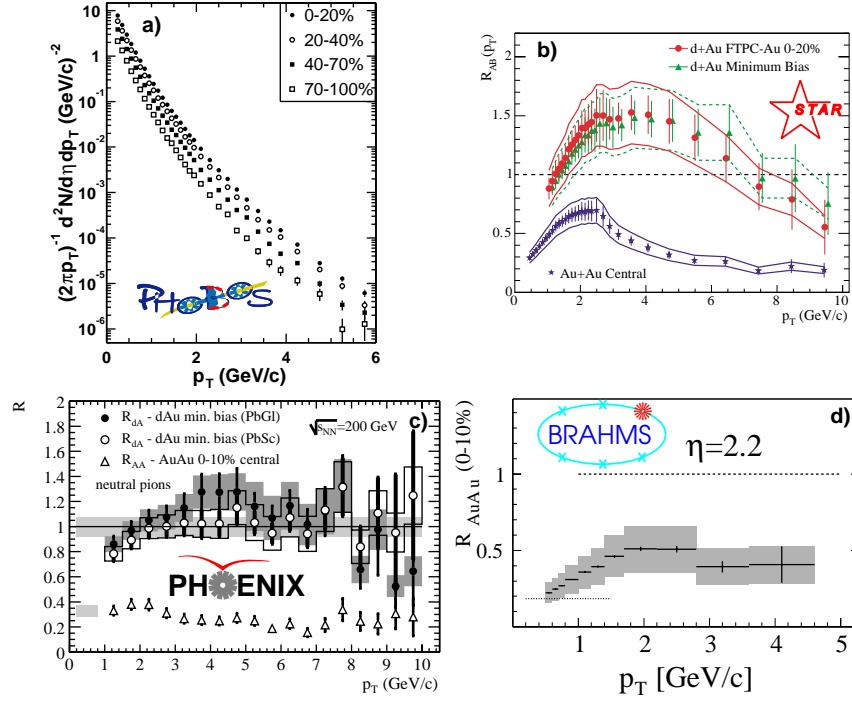


Fig. 15. *d+Au* and *Au+Au* measurements from PHOBOS [35], STAR [33], PHENIX [34] and BRAHMS [36].

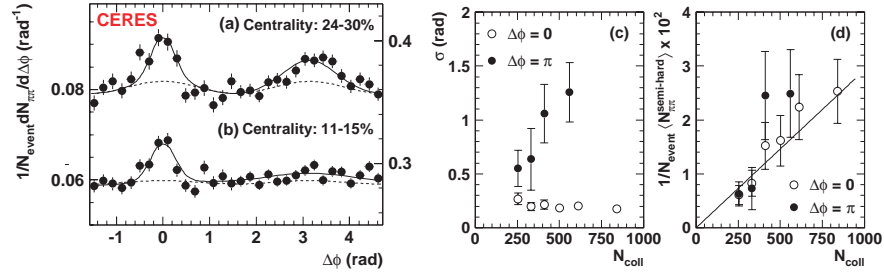


Fig. 16. Azimuthal correlations measured at the SPS by CERES [37].

top SPS energy. In Fig. 16a the nearside correlation (at $\Delta\phi = 0$) shows a narrow peak consistent with the correlation observed in jets. The away-side correlation peak is observed in more peripheral collisions but disappears for more central collisions, see Fig. 16b. Figure 16c shows that the width (σ) of the near-side correlation peak stays constant as a function of centrality, but that the away-side peak broadens for more central collisions. The total integrated

yield is the same in the near and away-side peak (Fig. 16d). Therefore, the disappearance of the away-side peak at the top SPS energy is interpreted as being due to initial state broadening [37].

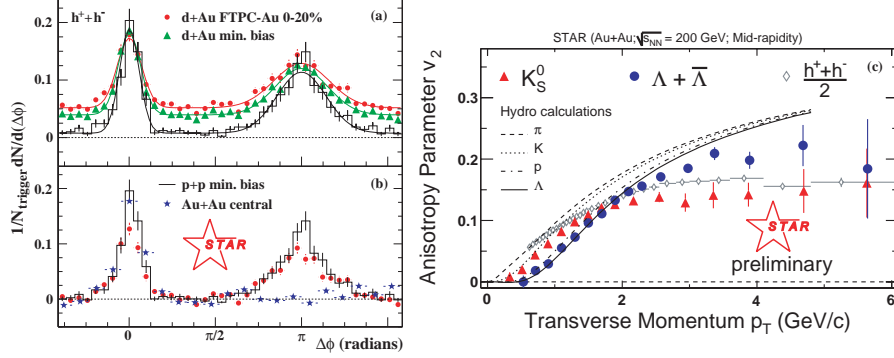


Fig. 17. *a,b*) Back to back correlations [38] and *c*) elliptic flow parameter [24] at intermediate p_t .

The azimuthal correlations of high- p_t particles (trigger particle $4 < p_t < 6$ GeV/ c , associated particle 2 GeV/ $c < p_t < p_t^{\text{trig}}$) measured in p+p collisions at RHIC are shown as the histogram in Fig. 17b. The near-side and away-side peaks are clearly visible. The correlation function observed in central Au+Au collisions (stars in Fig. 17b) shows a similar near side peak while the away-side peak has disappeared.

To investigate if this is due to initial state effects, the same analysis was done for d+Au collisions. In Fig. 17a the near and away-side peaks are shown for minimum bias and central d+Au collisions compared to p+p. The away-side correlation in d+Au is clearly observed even for the most central collisions. Comparing the away-side correlation in p+p, d+Au and Au+Au, Fig. 17b, shows that the suppression only occurs in Au+Au collisions and therefore is a final state effect as expected from jet quenching.

The energy loss depends on the distance traversed through the dense medium by the partons. In a non-central collision the distance will depend on the azimuthal angle with respect to the reaction plane [39] (see low- p_t section). Because the hard scattering producing the di-jet has no correlation with the reaction plane, an observed asymmetry in the high- p_t particle emission will be due to final state interactions (such as the jet quenching mechanism). In Fig. 17c the observed elliptic flow signal as a function of p_t is shown for charged particles, kaons and lambdas. It is clear from this figure that the observed asymmetry is very large up to the highest p_t measured. Like the nuclear suppression factor R_{AA} , the elliptic flow at intermediate p_t depends on the particle species. This could be due to an interplay between the soft

hydrodynamical behavior and the jet quenching, which would cause a mass dependence [40]. However, more recently this has been interpreted as a possi-

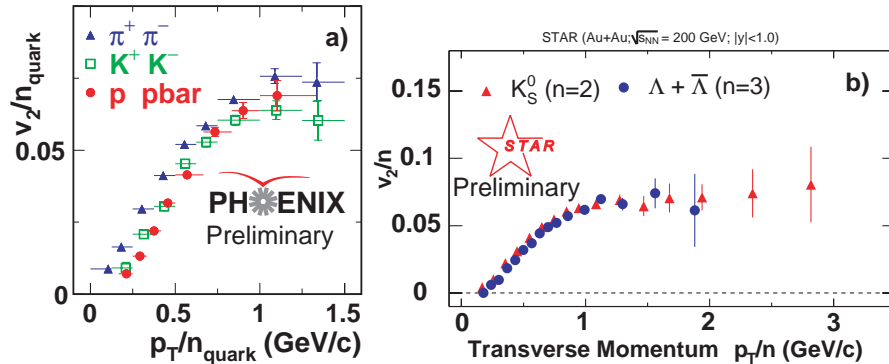


Fig. 18. *a)* Charged pion, charged kaon and proton plus antiproton v_2 measured by PHENIX [26]. *b)* K_S^0 and lambda plus antilambda v_2 measured by STAR [24]. Shown is v_2 versus p_t where both are normalized by the number of constituent quarks.

ble sign of particle production at intermediate p_t by parton coalescence [41]. In that case it is not the mass of the particle which is responsible for the splitting but rather the number of constituent quarks (two for mesons and three for baryons). Figure 18a,b shows the elliptic flow versus p_t , where both are normalized by the number of constituent quarks [26, 24]. Plotted like this, at intermediate p_t , the v_2 of the different species should reduce to an approximately universal curve. The measurement of the pions, kaons, protons and lambdas v_2 indeed seem to follow this scaling. A definitive test will be the measurement of elliptic flow of the ϕ -meson because in the coalescence interpretation it should have an elliptic flow similar to the pions while in the hydrodynamical interpretation it would have an elliptic flow value similar to the proton.

6 Conclusions

The first four years of RHIC operation have provided a wealth of interesting data. We have seen that:

- Particle yields indicate a chemical freeze-out of the system near the phase boundary;
- Identified particle spectra are consistent with boosted thermal distributions and identified particle elliptic flow shows remarkable agreement with ideal hydrodynamical calculations based on a QGP equation of state;

- The particle yield at high- p_t is suppressed compared to proton-proton reference data. The fact that this suppression does not occur in d+Au collisions shows that it is a final state effect, consistent with parton energy loss in dense matter (jet quenching);
- The suppression at intermediate p_t shows a particle dependence which could be explained by particle production, at intermediate p_t , by parton coalescence;
- The elliptic flow at intermediate p_t is large and also shows a particle dependence. Like above, this is consistent with energy loss in dense matter and particle production via parton coalescence;
- In the most central events the high- p_t back to back correlations are consistent with zero. Such disappearance of the away-side jets is expected in the case of very strong energy loss in a dense medium.

All these observations, taken together, are consistent with the creation of a very dense and strongly interacting system in heavy-ion collisions at RHIC energies. While all these observations are consistent with the creation of a QGP, more detailed knowledge of QCD at high densities and temperatures is required. This poses a formidable challenge for theory but will be crucial for the detailed interpretation of the present and future data taken at RHIC and LHC.

Acknowledgments

While preparing this presentation I heavily “borrowed” from other people whom I would like to thank: M. Baker, I. Bearden, J. Castillo, U. Heinz, T. Hemmick, P. Jacobs, P. Kolb, F. Laue, M. van Leeuwen, M. Lisa, G. Roland, P. Steinberg, A. Tang, N. Xu, W. Zajc and others I forgot.

References

1. F. Karsch, E. Laermann, hep-lat/0305025
2. Z. Fodor, S.D. Katz, JHEP 0203, (2002) 014
3. T. Roser, Nucl. Phys. **A698**, (2002) 23c
4. Nucl. Phys. **A499**, (2003) Issue 2-3
5. STAR collaboration, in preparation
6. K. Adcox *et al.*, Phys. Rev. Lett. **86**, (2001) 3500
7. K. Adcox *et al.*, Phys. Rev. Lett. **87**, (2001) 052301
8. J.D. Bjorken, Phys. Rev. **D27**, (1983) 140
9. B.B. Back *et al.*, Phys. Rev. Lett. **91**, (2003) 052303
10. I.G. Bearden *et al.*, Phys. Rev. Lett. **90**, (2003) 102301
11. P. Braun-Munzinger, D. Magestro, K. Redlich, J. Stachel, Phys. Lett. **B518** (2001) 41
12. P. Braun-Munzinger, J. Stachel, J. Phys. **G28** (2002) 1971

13. P. Braun-Munzinger, K. Redlich, J. Stachel, nucl-th/0304013
14. M. van Leeuwen for the NA49 collaboration, Nucl. Phys. **A715** (2003) 161
15. Thomas S. Ullrich, Nucl. Phys. **A715** (2003) 399
16. J. Adams *et al.*, nucl-ex/0310004
17. S.S Adler *et al.*, nucl-ex/0307022;
18. Barabara Wosiek for the PHOBOS collaboration, Nucl. Phys. **A715** (2003) 611
19. Djamel Ouerdane for the BRAHMS collaboration, Nucl. Phys. **A715** (2003) 478
20. C. Alt *et al.*, Phys. Rev. **C68** (2003) 034903
21. Peter F. Kolb and Ulrich Heinz, nucl-th/0305084. Pasi Huovinen, nucl-th/0305064; D. Teany, J. Lauret and E.V. Shuryak, nucl-th/01110037; Phys. Rev. Lett **86**, 4783 (2001).
22. P. Huovinen, P.F. Kolb, U. Heinz, Nucl. Phys. **A698** (2002) 475
23. C. Adler *et al.*, Phys. Rev. Lett. **87**, (2001) 182301
24. J. Adams *et al.*, nucl-ex/0306007
25. Raimond Snellings for the STAR collaboration, nucl-ex/0305001
26. ShinIchi Esumi for the PHENIX collaboration, Nucl. Phys. **A715** (2003) 599
27. R. Hanbury-Brown, R.Q. Twiss, Phil. Mag. Ser. 7, Vol. **45**, No. 366 (1954) 663, Nature **178** (1956) 1046
28. C. Adler *et al.*, Phys. Rev. Lett. **87**, (2001) 082301
29. S. Pratt, Phys. Rev. **D33**, (1986) 1314; S. Pratt, T. Csörgö, J. Zimanyi, Phys. Rev. **C42**, (1990) 2646; G. Bertsch, M. Gong, M. Tohyama, Phys. Rev. **C37**, (1988) 1896; U. Heinz, Nucl. Phys. **A610**, (1996) 264
30. Mike Lisa for the STAR collaboration, nucl-ex/0301005
31. M. Gyulassy and M. Plümer, Phys. Lett. **B243**, (1990) 432; R. Baier, D. Schiff and B.G. Zakharov, Annu. Rev. Nucl. Part. Sci. **B50**, (2000) 37; X.N. Wang and M. Gyulassy, Phys. Rev. Lett. **68**, (1992) 1480; X.N. Wang, Phys. Rev. **C58**, (1998) 2321
32. S.S. Adler *et al.*, nucl-ex/0304022
33. C. Adler *et al.*, Phys. Rev. Lett. **89**, (2002) 202301; J. Adams *et al.*, nucl-ex/0305015; J. Adams *et al.*, Phys. Rev. Lett. **91**, (2003) 072304
34. K. Adcox *et al.*, Phys. Rev. Lett. **88**, (2002) 022301; K. Adcox *et al.*, Phys. Lett. **B561** (2003) 82; S.S. Adler *et al.*, Phys. Rev. Lett. **91**, (2003) 072301; S.S. Adler *et al.*, Phys. Rev. Lett. **91**, (2003) 072303; S.S. Adler *et al.*, nucl-ex/0308006
35. B.B. Back *et al.*, Phys. Rev. Lett. **91**, (2003) 072302; B.B. Back *et al.*, nucl-ex/0302015
36. I. Arsene *et al.*, Phys. Rev. Lett **91**, (2003) 072305
37. G. Agakichiev *et al.*, nucl-ex/0303014
38. C. Adler *et al.*, Phys. Rev. Lett. **90**, (2003) 082302
39. R.J.M. Snellings, A.M. Poskanzer and S.A. Voloshin, nucl-ex/9904003; X.N. Wang, Phys. Rev. **C63**, (2001) 054902; M. Gyulassy, I. Vitev and X.N. Wang, Phys. Rev. Lett **86**, (2001) 2537; Miklos Gyulassy, Ivan Vitev, Xin-Nian Wang, Pasi Huovinen, Phys. Lett. **B526**, (2002) 301
40. T. Hirano and Y. Nara, nucl-th/0307015; X.-N. Wang, nucl-th/0305010
41. S.A. Voloshin, Nucl. Phys. **A715**, (2003) 379; D. Molnar, S.A. Voloshin, Phys. Rev. Lett. **91**, (2003) 092301; V. Greco, C.M. Ko and P. Levai, nucl-th/0305024; C. Nonaka, R.J. Fries, S.A. Bass, nucl-th/0308051